An Adaptive Subpixel Mapping Method Based on MAP Model and Class Determination Strategy for Hyperspectral Remote Sensing Imagery

Yanfei Zhong, *Member, IEEE*, Yunyun Wu, Xiong Xu, and Liangpei Zhang, *Senior Member, IEEE*

Abstract—The subpixel mapping technique can specify the spatial distribution of different categories at the subpixel scale by converting the abundance map into a higher resolution image, based on the assumption of spatial dependence. Traditional subpixel mapping algorithms only utilize the low-resolution image obtained by the classification image downsampling and do not consider the spectral unmixing error, which is difficult to account for in real applications. In this paper, to improve the accuracy of the subpixel mapping, an adaptive subpixel mapping method based on a maximum *a posteriori* (MAP) model and a winner-take-all class determination strategy, namely, AMCDSM, is proposed for hyperspectral remote sensing imagery. In AMCDSM, to better simulate a real remote sensing scene, the low-resolution abundance images are obtained by the spectral unmixing method from the downsampled original image or real low-resolution images. The MAP model is extended by considering the spatial prior models (Laplacian, total variation (TV), and bilateral TV) to obtain the high-resolution subpixel distribution map. To avoid the setting of the regularization parameter, an adaptive parameter selection method is designed to acquire the optimal subpixel mapping results. In addition, in AMCDSM, to take into account the spectral unmixing error in real applications, a winner-take-all strategy is proposed to achieve a better subpixel mapping result. The proposed method was tested on simulated, synthetic, and real hyperspectral images, and the experimental results demonstrate that the AMCDSM algorithm outperforms the traditional subpixel mapping methods and provides a simple and efficient algorithm to regularize the ill-posed subpixel mapping problem.

Index Terms—Adaptive, hyperspectral image, maximum *a posteriori* (MAP), remote sensing, spectral unmixing, subpixel mapping, winner-take-all strategy.

I. INTRODUCTION

HYPERSPECTRAL remote sensing images can provide luxuriant spectral information [1]. However, because of the impact of the sensor's instantaneous field-of-view and the

Y. Zhong, Y. Wu, and L. Zhang are with the State Key Laboratory of Information Engineering in Surveying, Mapping and Remote Sensing, Wuhan University, Wuhan 430079, China (e-mail: zhongyanfei@whu.edu.cn; wenwubei@whu.edu.cn; zlp62@whu.edu.cn).

X. Xu is with the College of Surveying and Geo-Informatics, Tongji University, Shanghai 200092, China (e-mail: xvxiong@tongji.edu.cn).

diversity of the land-cover classes [1], the mixed pixel is a common phenomenon in hyperspectral remote sensing images. Soft classification and spectral unmixing techniques [2], which can estimate the proportion of every endmember inside a pixel at a subpixel scale and yield a series of abundance maps of the different categories [3]–[5], are often utilized to solve the mixed pixel problem. However, they still do not divulge any subpixel spatial distribution information for each endmember within a pixel, and this subpixel information is very important in real applications such as classification and target detection. To obtain the spatial distribution of the different categories of subpixels, the subpixel mapping method [6], [7] based on the assumption of spatial dependence was proposed, which can divide a pixel into several smaller subpixels in a finer resolution, according to the subpixel mapping scale, and assigns a certain land-cover class to each subpixel, based on the abundance fractions [6].

Various subpixel mapping algorithms have been proposed. The artificial neural network subpixel mapping algorithms, e.g., the Hopfield neural network [8]–[11], the back-propagation (BP) neural network [12], [13], and the multilayer perceptron neural network [14], have been successfully used for remote sensing imagery. Verhoeye *et al.* [15] used a linear optimization technique to solve the subpixel mapping problem by transforming the issue into an optimization problem. Mertens *et al.* [16] proposed a simple but effective method based on subpixel/pixel spatial attraction models to satisfy the requirement of spatial dependence. Atkinson *et al.* [17] presented a pixel-swapping algorithm, which can exchange subpixels to obtain the optimal result. Recently, subpixel mapping algorithms based on computational intelligence, e.g., genetic algorithms [18], differential evolution [19], artificial immune systems [20], multiagent systems [21], and particle swarm optimization [22], have been successfully applied for remote sensing imagery. In addition, Markov random fields (MRFs) [23]–[25], geostatistical methods [26]–[28], geometric subpixel mapping algorithm [29], and interpolation-based methods [30] have also been proposed.

Most of the aforementioned methods are based on the spatial dependence assumption [31], in which observations close together are more alike than those further apart, where this assumption is fulfilled on the condition that the intrinsic scale of the spatial variation in each land-cover class is not smaller than the sampling scale imposed by the image pixels [7]. Although the MRF models [23]–[25] and geostatistics [26]–[28] can be extended to incorporate various spatial patterns into

the subpixel mapping, most of the aforementioned methods do not always truly reflect the spatial pattern of subpixels in real applications. In fact, subpixel mapping can be recognized as an inverse or ill-posed problem which reconstructs a fine-resolution map from a series of low-resolution abundance maps [32]. Consequently, a regularized method based on a maximum *a posteriori* (MAP) model has been proposed to solve the ill-posed subpixel mapping problem, due to the advantages of expansibility and the ease of adding prior information [33], in which it can be applied to describe the relationship between the abundance map and the spatial distribution image of the subpixels, and the MAP algorithm can obtain the final result of the high-resolution (HR) distribution image. However, multiple shifted images are required in the algorithm proposed in [33], and the regularization parameter needs to be defined in advance, which often cannot be achieved in real applications. In addition, as in most of the traditional methods, the abundance map of the different classes utilized in the previous MAP-based subpixel mapping algorithm [33] is obtained by downsampling a classification image without spectral unmixing errors, and it is still difficult to process a real remote sensing image [19].

To solve these problems and improve the subpixel mapping accuracy for real applications, an adaptive subpixel mapping method based on a MAP model and a winner-take-all class determination strategy (AMCDSM) is proposed for hyperspectral remote sensing images. In AMCDSM, the MAP model is utilized to solve the subpixel mapping problem for hyperspectral remote sensing images, in which the ill-posed subpixel mapping problem is transformed to be well-posed. Differing from the user-defined parameter setting in MAP subpixel mapping with multiple shifted hyperspectral images (MMSSM) [33], AMCDSM with a single image can adaptively obtain the regularization parameter. In addition, to better simulate a real scene, the input abundance images are obtained by unmixing the downsampled original image in AMCDSM, not by downsampling a classification image, as in [33]. The AMCDSM method can adaptively reduce the influence of the spectral unmixing errors by adding the prior information of the spatial pattern as a constraint in the MAP model and winner-take-all strategy as follows.

1) *Spatial regularization constraint*. In the proposed AMCDSM framework, the subpixel mapping problem can be transformed into a regularization problem, and the MAP model is applied to regularize the subpixel mapping problem by reconstructing a classification map with a higher resolution from the abundance images with a lower resolution. In this paper, three prior models, namely, Laplacian [34], total variation (TV) [35], and bilateral TV (BTV) [36], are applied, respectively. The spatial regularization constraint of the MAP model attains a smooth solution and effectively reduces the noise problem.

2) *Self-adaptive regularization parameter control*. The regularization parameter is a tradeoff between the data fidelity and the prior item, and it controls the balance between the fidelity of the data and the smoothness of the solution. To improve the adaptability of AMCDSM, the regularization parameter is adaptively updated based on

different abundance images to find the optimal solution. An adaptive parameter control method [37] is applied in the MAP-based subpixel mapping model, with three prior regularization models, to select the optimal regularization parameter adaptively, accurately, and efficiently.

3) *Winner-take-all class determination strategy*. In AMCDSM, to better avoid the impact of the spectral unmixing errors, a winner-take-all class determination strategy is utilized, taking into account the spatial information between subpixels, which can produce a smooth result. The MAP result represents the HR MAP image for the different classes. According to the winner-take-all strategy, the subpixel belongs to the class with the maximum value.

The AMCDSM method was tested and compared with the traditional algorithms, using a simulated hyperspectral image, three synthetic hyperspectral images, and a real Nuance hyperspectral image. The experimental results demonstrate that the proposed model can adaptively obtain a better result and a higher subpixel mapping accuracy for hyperspectral remote sensing imagery.

The rest of this paper is organized as follows. Section II presents the necessary background information about the subpixel mapping problem. In Section III, the proposed adaptive subpixel mapping method based on a MAP model and a winner-take-all class determination strategy (AMCDSM) is described in detail. Section IV describes the experimental results and analyses. A sensitivity analysis is also provided in this section. Finally, the conclusion is provided in Section V.

II. BACKGROUND

A. Basic Principles of Subpixel Mapping

Subpixel mapping techniques aim to determine the optimal distribution of subpixels of the different land-cover classes within a pixel, based on the fraction images. The fractions of each category can be obtained by a spectral unmixing technique [38]. Subpixel mapping can be achieved by using spatial dependence assumptions, and it was first proposed by Atkinson in 1997, inspired by Tobler's first law [39]. This refers to the tendency for spatially proximate observations of a given property to be more alike than more distant observations [6]. Subpixel mapping can transform the fraction image into a map of suitable subpixel locations for the different classes within a pixel. Each pixel can be divided into a number of subpixels during this transformation, according to the predefined scale S and the abundances of the fraction image.

Fig. 1 shows the basic principle of subpixel mapping and describes a simple example with three classes. As shown in Fig. 1(a), the pictures of the trees represent three different classes, corresponding to Fig. 1(b)–(d), and the three values represent the fractions of the three different categories, corresponding to the central pixel (mixed pixel) in Fig. 1(b). The fractions of the three different categories can be obtained by spectral unmixing, and the values in Fig. 1(b) represent the fractions of each pixel. In Fig. 1(b), each pixel is divided into
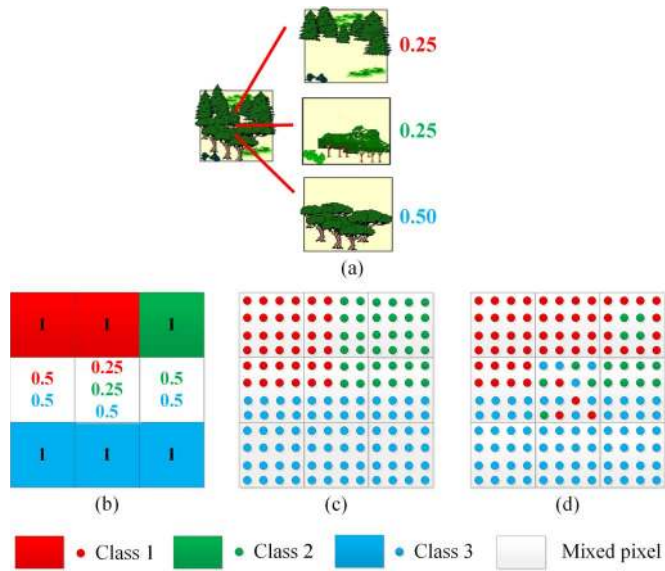
Fig. 1. Example of subpixel mapping (3 × 3 coarse pixels, S = 4, and 3 classes). (a) Original image and the fractions of the central pixel in (b). (b) Fraction image. (c) Possible distribution. (d) Another possible distribution.

16 (4 × 4) subpixels, with the assumption that the scale S is 4, and the red, green, and blue squares represent the pure pixels, while the white squares represent the mixed pixels of different classes, respectively. In addition, the values in red, green, and blue colors represent the fractions of land-cover classes 1, 2, and 3, respectively; for example, 0.5 in blue means that there are 8 (4 × 4 × 0.5) subpixels belonging to class 3. Fig. 1(c) and (d) illustrates two possible distributions of the subpixels. According to the assumption of spatial dependence, the former is superior to the latter.

B. Construction of the Subpixel Mapping Observation Model

In this paper, the subpixel mapping problem is transformed into a regularization problem, and the MAP model is applied to regularize the subpixel mapping problem to be well-posed. The MAP model can obtain the optimal result for the HR pixels (subpixels). Meanwhile, the MAP result represents the HR MAP image for the different classes. The MAP model, as mentioned before, has the advantages of expansibility and the ease of adding prior information and can be used to solve the subpixel mapping problem.

In order to build the subpixel mapping observation model, the impact of the downsampling matrix is considered. The purpose of subpixel mapping is to convert the low-resolution fraction (LRF) images to an HR classification (HRC) map by looking for the optimal distribution of objects at the subpixel scale. For different fraction images of different classes, the final result is the distribution of each class in the HRC image. Thus, the observation model can be considered as shown in Fig. 2, where y^c is the fraction image of class c and x^c is the result of the subpixel mapping on the corresponding central pixel in green color. The subpixel mapping scale is set to be 3. The coordinate system is shown in Fig. 2, where the red color represents the coordinates of each pixel or subpixel. In addition, the coordinate values of each subpixel shown in green
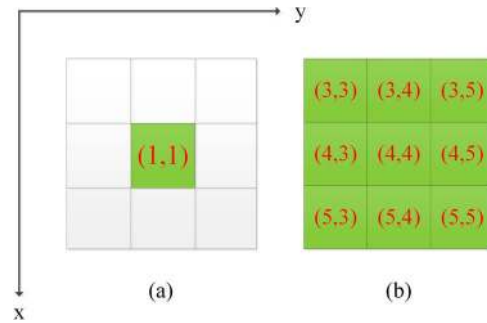

Fig. 2. Observation model of subpixel mapping. (a) y^c, the fraction image of class c. (b) x^c, the result of the subpixel mapping on the central pixel.

color in Fig. 2(b) represent the corresponding central pixel in green color in Fig. 2(a), and the coordinates of Fig. 2(a) and (b) are unified into the same coordinate system. Because this is a single-class mapping problem, y^c is an image of value 0–1, and a value of 1 for the subpixel means that it belongs to category c. The mapping model is shown in

$$
\begin{aligned}
y^c(1,1) = {} & \frac{1}{9} \times x^c(3,3) + \frac{1}{9} \times x^c(3,4) + \frac{1}{9} \times x^c(3,5) \\
& + \frac{1}{9} \times x^c(4,3) + \frac{1}{9} x^c(4,4) + \frac{1}{9} \times x^c(4,5) \\
& + \frac{1}{9} \times x^c(5,3) + \frac{1}{9} \times x^c(5,4) + \frac{1}{9} \times x^c(5,5)
\end{aligned}
$$

$$
= \left[\frac{1}{9}\frac{1}{9}\frac{1}{9}\frac{1}{9}\frac{1}{9}\frac{1}{9}\frac{1}{9}\frac{1}{9}\frac{1}{9} \right]
\begin{bmatrix}
x^c(3,3) \\
x^c(3,4) \\
x^c(3,5) \\
x^c(4,3) \\
x^c(4,4) \\
x^c(4,5) \\
x^c(5,3) \\
x^c(5,4) \\
x^c(5,5)
\end{bmatrix}
$$

$$
= \left[\frac{1}{S^2}\ \frac{1}{S^2}\ \frac{1}{S^2}\ \frac{1}{S^2}\ \frac{1}{S^2}\ \frac{1}{S^2}\ \frac{1}{S^2}\ \frac{1}{S^2}\ \frac{1}{S^2} \right]
\begin{bmatrix}
x^c(3,3) \\
x^c(3,4) \\
x^c(3,5) \\
x^c(4,3) \\
x^c(4,4) \\
x^c(4,5) \\
x^c(5,3) \\
x^c(5,4) \\
x^c(5,5)
\end{bmatrix} \quad (1)
$$

where $y^c(1,1)$ is the fraction value of the pixel in coordinate (1,1), i.e., the central pixel in Fig. 2(a). $x^c(3,3), x^c(3,4), x^c(3,5), x^c(4,3), \ldots, x^c(5,5)$ represent the different subpixel values in the mapping result. The coefficient 1/9 is related to the reconstruction scale. Based on this method, the observation model can be constructed for each pixel in the LRF image; then, a series of observation equations can be created. Then, for each category, the observation model between the fraction images and the subpixel result can be constructed

$$
y^c = Dx^c + n^c \quad (2)
$$

where D is the downsampling matrix, which is related to the reconstruction scale. y^c is the fraction image of class c, in which

the values are 0–1. x^c is the result of the subpixel mapping on class c, which can take on a value between 0 and 1, and n^c is the additive noise. In addition, c represents the different categories.

III. ADAPTIVE SUBPIXEL MAPPING METHOD BASED ON A MAP MODEL AND A WINNER-TAKE-ALL CLASS DETERMINATION STRATEGY

In this paper, an adaptive subpixel mapping method based on a MAP model and a winner-take-all class determination strategy (AMCDSM) is proposed for hyperspectral remote sensing imagery. The subpixel mapping problem can be formulated as an ill-posed problem which does not have a unique number of solutions. In AMCDSM, the ill-posed subpixel mapping problem is transformed into a regularization problem. The MAP model with spatial prior information, e.g., Laplacian, TV, and BTV prior models, is designed to build the HR subpixel mapping results, using a series of LRF images, based on the advantage of a MAP model, i.e., the unique solution, expansibility, and ease of adding prior information. By incorporating the spatial distribution prior into the subpixel mapping, this can better reduce the spectral unmixing errors. The regularization parameter can be obtained using an adaptive method. In the proposed method, the LRF image can be adaptively converted to an HRC map. Subsequently, the winner-take-all strategy is utilized to obtain the final subpixel mapping result.

AMCDSM consists of the following steps.

A. MAP-Based Subpixel Mapping Observation Model

In this paper, a MAP method is utilized to regularize the subpixel mapping problem to be well-posed by adding three prior models, i.e., Laplacian, TV, and BTV. Based on the mapping model in (2), the MAP approach seeks the $\hat{x}^c_{\text{MAP}}$ to estimate x^c as (3), for which the *a posteriori* probability $\Pr(x^c|y^c)$ is the maximum

$$\hat{x}^c_{\text{MAP}} = \arg \max \left\{ \Pr(x^c|y^c) \right\}. \tag{3}$$

Applying Bayes' rule

$$\hat{x}^c_{\text{MAP}} = \arg \max \left\{ \frac{\Pr(y^c|x^c)\Pr(x^c)}{\Pr(y^c)} \right\}. \tag{4}$$

As $\Pr(y^c)$ is a constant and has no effect on the results, it can be removed

$$\hat{x}^c_{\text{MAP}} = \arg \max \left\{ \Pr(y^c|x^c)\Pr(x^c) \right\}. \tag{5}$$

Applying the monotonic logarithm function to (5), it can then be shown as

$$\hat{x}^c_{\text{MAP}} = \arg \max \left\{ \log \Pr(y^c|x^c) + \log \Pr(x^c) \right\} \tag{6}$$

where $\Pr(y^c|x^c)$ is the likelihood function of the LRF image for class c and $\Pr(x^c)$ is the prior density of the image x^c.

Assuming that the image noise is Gaussian noise with zero mean and the same variance σ, $\Pr(y^c|x^c)$ can be shown as

$$\Pr(y^c|x^c) = \prod_{\forall x,y} \frac{1}{\sigma\sqrt{2\pi}} \exp\left(-\frac{(\hat{y}^c - y^c)^2}{2\sigma^2}\right). \tag{7}$$

While the prior $\Pr(x^c)$ is subjected to the Gibbs form

$$\Pr(x^c) = \frac{1}{\rho} \exp\left(-\frac{1}{\beta}U(x^c)\right) \tag{8}$$

where ρ is a constant, β is a control parameter, and $U(x^c)$ is the energy function.

Substituting (7) and (8) in (6) yields

$$\hat{x}^c_{\text{MAP}} = \arg \max \left\{ \log \frac{(\sigma\sqrt{2\pi})^{-N}}{\rho} \right.$$
$$\left. - \sum \frac{(\hat{y}^c - y^c)^2}{2\sigma^2} - \frac{1}{\beta}U(x^c) \right\}. \tag{9}$$

The first term on the right of the equation is a constant, which can be directly eliminated, and the remaining two negative terms can be transferred to positive ones; thus, the maximization problem is transformed into the following minimization problem:

$$\hat{x}^c_{\text{MAP}} = \arg \min \left\{ \sum (\hat{y}^c - y^c)^2 + \frac{2\sigma^2}{\beta}U(x^c) \right\}. \tag{10}$$

Assuming that $\lambda = 2\sigma^2/\beta$, representing the regularization parameter, we then substitute (2) into (10)

$$\hat{x}^c_{\text{MAP}} = \arg \min \left\{ \|y^c - Dx^c\|^2 + \lambda U(x^c) \right\}. \tag{11}$$

In this equation, the first term is the data fidelity term, which constrains the numerical relationship between the HR distribution image and the LR fraction image, and the second term is a prior term, which describes the spatial distribution pattern of the HR image. λ is the weight or regularization parameter used to control the balance of the data fidelity term and the prior term.

B. Preprocessing in AMCDSM

To simulate a real application, the input synthetic images are degraded using ENVI software [40] at a suitable scale so that the downsampled original images can be obtained. A spectral unmixing method is then utilized to obtain the abundance fraction image of each class or endmember of the original input data.

The nearest neighbor interpolation method [41] is applied to the LRF image to obtain the initial HR distribution image. As the degradation scale is known and the low-resolution images and the initial HR image have been obtained, the observation model for the subpixel mapping can be constructed using (2).

C. Adaptive MAP Model Solution

As the observation model of the subpixel mapping has been constructed, AMCDSM can solve the problem according to the following steps.

Step 1—Adaptive Regularization Parameter Selection: In (11), the regularization parameter λ controls the balance between the fidelity term $\|y - Dx\|^2$ and the prior term $U(x)$. If the parameter is too small, the noise problem cannot be

effectively solved. Alternatively, if the parameter is too large, the result will be too smooth, and there will be a loss of details. Consequently, the selection of the regularization parameter is critical for the subpixel mapping result. In the conventional algorithms, the regularization parameter is chosen as a fixed numerical value from a set of candidate values. The optimal result is then selected from the candidate values by comparing all of the results. Choosing an optimal parameter is particularly difficult because the regularization parameter is decided by the prior information. In most applications, an accurate estimation of the prior information is difficult to obtain. In addition, the manually defined parameter method is complicated and time-consuming and is prone to missing the optimal solution.

To solve the aforementioned problems, an adaptive parameter selection method is proposed. In the adaptive method, the regularization parameter is estimated at the same time as the iteration when obtaining the HR distribution map. The method makes full use of the iterative intermediate reconstruction information to update the parameter λ. The newly acquired image is applied to the next iteration to obtain a new λ, and the optimal solution is eventually acquired.

The following properties of λ are incorporated in the proposed algorithm [37].

1) $\lambda > 0$. As is shown in the regularization principle, a regularization parameter of less than zero is meaningless; it must be larger than zero.
2) λ is proportional to $\|y - Dx\|^2$. As the value of $\|y - Dx\|^2$ increases, the noise contained in the model enlarges, and it requires a larger λ to regularize the problem and eliminate the impact of noise on the results. Consequently, λ is proportional to $\|y - Dx\|^2$.
3) λ is inversely proportional to $U(x)$. The edge and texture details of the image will be more abundant as the value of $U(x)$ increases. To avoid the oversmoothing phenomenon, a smaller regularization parameter is selected. Therefore, λ is inversely proportional to $U(x)$.

To satisfy the aforementioned conditions, the proposed regularization function can be described as

$$\lambda_{k+1} = \ln\left(\mu\frac{\|y - Dx_k\|^2}{U(x) + r} + 1\right) \tag{12}$$

where λ_{k+1} is the regularization parameter of the $k + 1$ iteration; x_k is the subpixel reconstruction map obtained in the kth iteration; $U(x)$ is the prior model, which is presented in the next part; r is the control parameter, which prevents the denominator from being zero; and μ is the modified factor of λ, which can select a fixed value.

Step 2—The Solution of the Spatial Regularization Terms: The prior model $U(x^c)$ plays an important role in the proposed method. It can regularize the ill-posed problem to obtain a stable unique solution [42]. Many different prior models have been proposed in recent years, such as the Gaussian MRF model [43], the Huber-MRF model [44], the weighted-MRF model [45], the sparse directional regularization [46], the Laplacian model [34], the TV model [35], and the BTV model [36]. In AMCDSM, the prior model is assumed to be the same for each category, and Laplacian, TV, and BTV prior models are used to

test the performance of the proposed method. The three prior models are described as follows.

a) Laplacian prior model: The Laplacian prior model is derived from the Tikhonov regularization method. It is a 2-D Laplacian matrix which can put a constraint on the high-frequency component of an ill-posed problem so as to provide a smooth solution to the problem. The energy function is usually defined as

$$U(x^c) = \|\mathbf{Q}x^c\|_2^2 \qquad 0 \le x^c \le 1 \tag{13}$$

where Q is the Laplacian matrix.

b) TV prior model: The TV prior model has the advantage of being able to better maintain the edges and detailed information of the image and can be represented as

$$U(x^c) = \sum_i \sum_j \sqrt{|\nabla x_h^c|^2 + |\nabla x_v^c|^2} \tag{14}$$

where ∇x_h^c and ∇x_v^c are linear operators representing the gradient along the horizontal and vertical directions of the image x^c, which can be computed as

$$\nabla x_h^c = x^c[i+1, j] - x^c[i, j]$$
$$\nabla x_v^c = x^c[i, j+1] - x^c[i, j] \qquad 0 \le x^c \le 1. \tag{15}$$

c) BTV prior model: The BTV prior model is derived from the TV prior by adding a bilateral filter. The l_1 form of TV is a special case of BTV. The BTV prior is better at preserving the edges of the image and is computationally efficient to realize. The expression of BTV can be shown as [33], [35]

$$U(x^c) = \sum_{l=-P}^{P} \sum_{m=0}^{P} \alpha^{|m|+|l|} \left\|x^c - \mathbf{S}_h^l \mathbf{S}_v^m x^c\right\|_1 \quad 0 \le x^c \le 1 \tag{16}$$

where matrices $\mathbf{S}_h^l$ and $\mathbf{S}_v^m$ shift the image x^c by l and m pixels horizontally and vertically, respectively. The parameter α, $0 < \alpha < 1$, is the scale weighting parameter and can be used to give a spatially decaying effect to the summation of the regularization terms [36].

After the prior model and the adaptive regularization parameter are determined, the MAP iteration result for each class can be obtained by minimizing the following objective function:

$$E(x^c) = \|y^c - Dx^c\|^2 + \lambda U(x^c). \tag{17}$$

In order to obtain the minimized value of (17), the gradient descent [34] method is utilized. Differentiating (17) with respect to x^c, we have

$$\nabla E(x^c) = -2D^T(y^c - Dx^c) + \lambda \nabla U(x^c) \tag{18}$$

where $\nabla U(x^c)$ can be calculated as

$$\text{Laplacian}: \quad \nabla U(x^c) = 2Q^T Q x^c \tag{19}$$

$$\text{TV}: \quad \nabla U(x^c) = \sum_i \sum_j \nabla \cdot \left(\frac{[\nabla x_h^c \quad \nabla x_v^c]^T}{\sqrt{|\nabla x_h^c|^2 + |\nabla x_v^c|^2 + \beta}}\right) \tag{20}$$
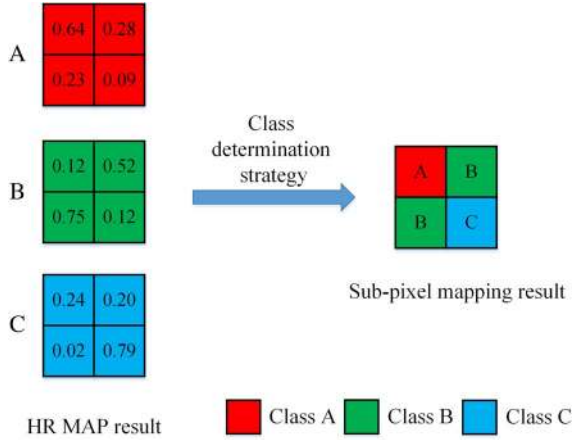
Fig. 3. Winner-take-all class determination strategy of subpixel mapping.

$$\text{BTV}: \quad \nabla U(x^c) = \sum_{l=-P}^{P} \sum_{m=0}^{P} \alpha^{|m|+|l|} \left[I - (S_h^l)^T (S_v^m)^T \right]$$
$$\times \operatorname{sign}\left(x^c - S_h^l S_v^m x^c \right). \tag{21}$$

In these equations, $\nabla \cdot ()$ represents the divergence operator, and β is a small positive parameter which ensures the differentiability of the equation. $\left(S_h^l\right)^T$ and $\left(S_v^m\right)^T$ are the transposes of S_h^l and S_v^m, and they play a role in shifting the image in the opposite direction to S_h^l and S_v^m.

Due to the influence of the singular matrix and the large computation time required, the MAP model can be solved by an iterative computation sequence. The iteration equation can be displayed as

$$\hat{x}_{n+1}^c = \hat{x}_n^c + 2D^T(Dx^c - y^c) + \lambda \nabla U(\hat{x}^c). \tag{22}$$

A fixed iteration number is chosen as the iteration termination condition.

D. Winner-Take-All Class Determination Strategy

In the proposed method, the original image downsampling and spectral unmixing are used to obtain the abundance maps of the different classes [47]–[49]. This process is influenced by the spectral unmixing errors. If, when generating the subpixel mapping result, the integration of the HR image is in strict accordance with the abundance fractions, the spatial information between subpixels will be lost. Hence, a winner-take-all class determination strategy is proposed to solve the problem.

In the MAP iteration, all of the HR results x^c for each class c are obtained and integrated to acquire the HRC image x. Assuming that a coarse pixel is divided into S × S subpixels in x^c, then every pixel value should be normalized to [0, 1] because the value represents the fraction of a subpixel of a certain class c. Assuming that the class of a subpixel is z, it must satisfy the condition that $x^z = \max\{x^c | c = 1, 2, \ldots, C\}$, where $\sum_{c=1}^{C} x^c = 1$ and C is the number of classes. The subpixel mapping result can be obtained by utilizing this winner-take-all class determination strategy. The process is described in Fig. 3. As is shown in Fig. 3, A, B, and C represent three classes, in red, green, and blue colors, respectively. In addition,

the values are the MAP result of each subpixel, representing the HR distribution information, and the scale is 2. According to the winner-take-all strategy, the values (which represent the probabilities of the subpixels belonging to a certain class) of each pixel for every class in the same position need to be compared, such as 0.64 for class A, 0.12 for class B, and 0.24 for class C. Here, the maximum value is 0.64 for class A, so the subpixels in the left corner belong to class A.

All of the processes are shown as a flowchart of AMCDSM in Fig. 4. As shown in Fig. 4, the input fraction images are obtained by unmixing the LR image (which can be obtained by downsampling or collected by the original LR image), to which the probabilistic support vector machine (P-SVM) [49] and fully constrained least squares (FCLS) spectral unmixing methods are applied. The fraction images are applied to the MAP model to acquire the HR MAP result. Finally, the subpixel mapping result is obtained by utilizing the winner-take-all class determination strategy.

IV. EXPERIMENTS AND ANALYSES

One simulated image, three synthetic images, and one real image were used to test the AMCDSM algorithm with Laplacian, TV, and BTV prior models, namely, AMCDSM-L, AMCDSM-TV, and AMCDSM-BTV. These methods were compared with the traditional subpixel mapping methods of nearest neighbor interpolation based subpixel mapping (NNISM), subpixel mapping based on a spatial attraction model (SASM) [16], pixel-swapping subpixel mapping algorithm (PSSM) [17], BP neural network subpixel mapping method (BPSM) [12], [13], subpixel mapping based on a genetic algorithm (GASM) [18], and geometric subpixel mapping algorithm (GSM) [29].

A. Data Preparation and Accuracy Assessment

In the experiments, the proposed algorithm should ideally be applied on fraction images at a certain scale and compared with the results of a hard classification at a finer resolution. To avoid the uncertainty inherent in real imagery that is caused by the sensor point spread function, atmospheric and geometric effects, and classification or spectral unmixing errors [18], simulated and synthetic images were used in the first four experiments. The hard classification image obtained by the classifier was regarded as the reference image. The input abundance fraction images with a coarser scale were obtained by unmixing the downsampled original hyperspectral remote sensing data, to which the P-SVM [49] and FCLS spectral unmixing methods were applied. Simulated and synthetic imageries have the advantage of lacking coregistration errors between the lower and higher resolution images. Consequently, the subpixel mapping results of the simulated and synthetic images can better reflect the performance of the proposed methodology. For these simulated and synthetic images, the scale factor was set to 4.

Although simulated and synthetic images can avoid the errors of coregistration, our current study also aims to apply the subpixel mapping technique to real imagery. Therefore, real imagery obtained from a Nuance hyperspectral imaging camera
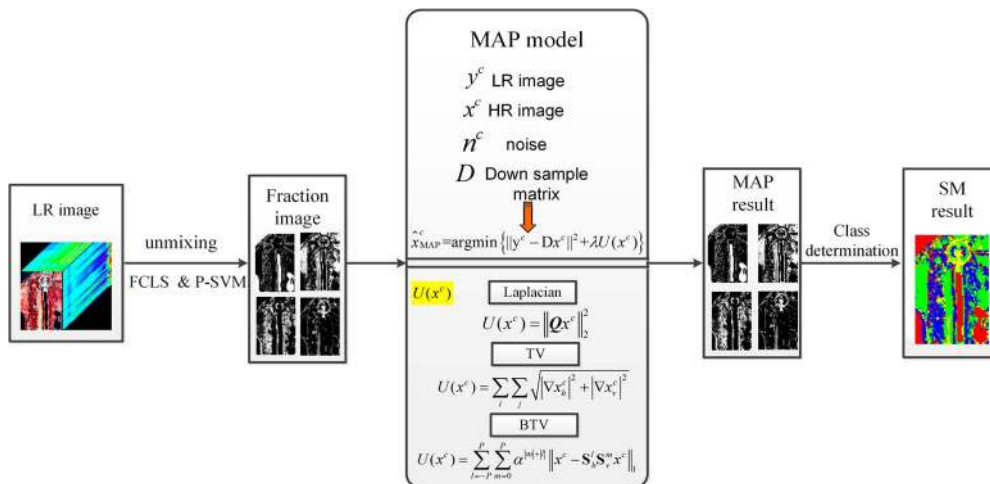
Fig. 4. Flowchart of the adaptive subpixel mapping method based on a MAP model and class determination strategy.
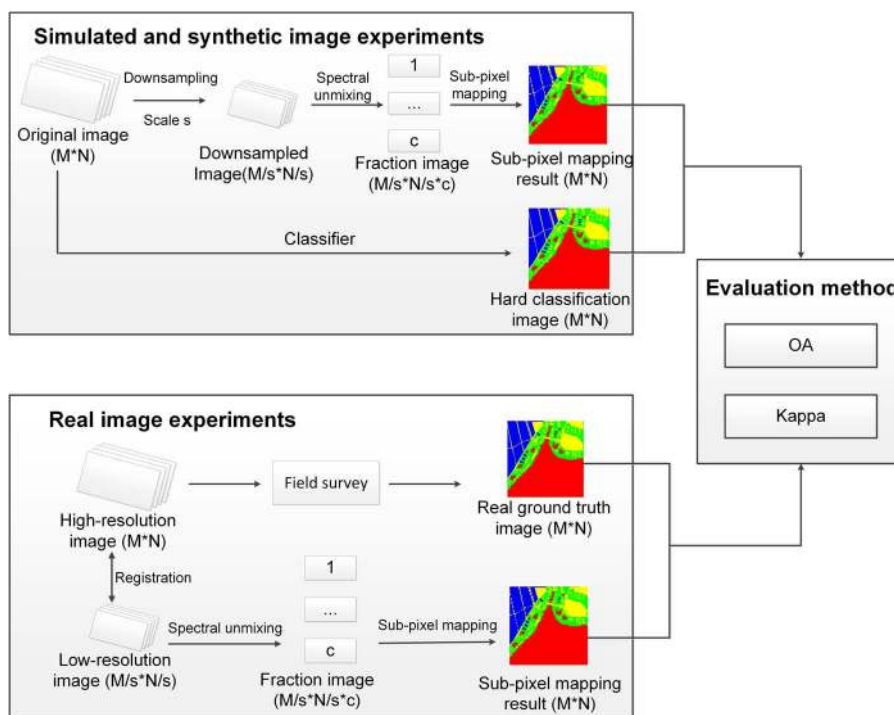

Fig. 5. Experimental process of the subpixel mapping algorithm.

was utilized to test the performance of the subpixel mapping algorithm.

The experimental process of the subpixel mapping algorithm is shown in Fig. 5. As shown in Fig. 5, for the simulated and synthetic image experiments, the downsampled image was obtained by downsampling the original image, given a fixed scale. FCLS and P-SVM were then utilized to acquire the fraction images of the different classes. The adaptive MAP-based subpixel mapping algorithm was then used to obtain the final subpixel mapping result. An accuracy evaluation was undertaken by making a comparison with the classification map obtained by classifying the original image. Furthermore, for the real image experiment, the LR image was obtained by the use of a Nuance NIR imaging spectrometer, and then, the spectral unmixing method was applied to obtain the fraction

images. Finally, the subpixel mapping result was acquired using the adaptive MAP-based method. An accuracy evaluation was then obtained by making a comparison with the real reference ground truth classification map, which was obtained by a digital camera for the same area as the LR image.

As mentioned before, the accuracy was measured by comparing the results of the subpixel mapping with the reference classification map. Unlike the simulated experiments, more error sources were introduced in the original downsampling method, including the downsampling errors, the spectral unmixing error of the LRF image, the error of the subpixel mapping methods, and the registration error of the LRF image and the HRC map. Two accuracy evaluation indices, the overall accuracy (OA) and kappa coefficient, were used to test the subpixel mapping accuracy.
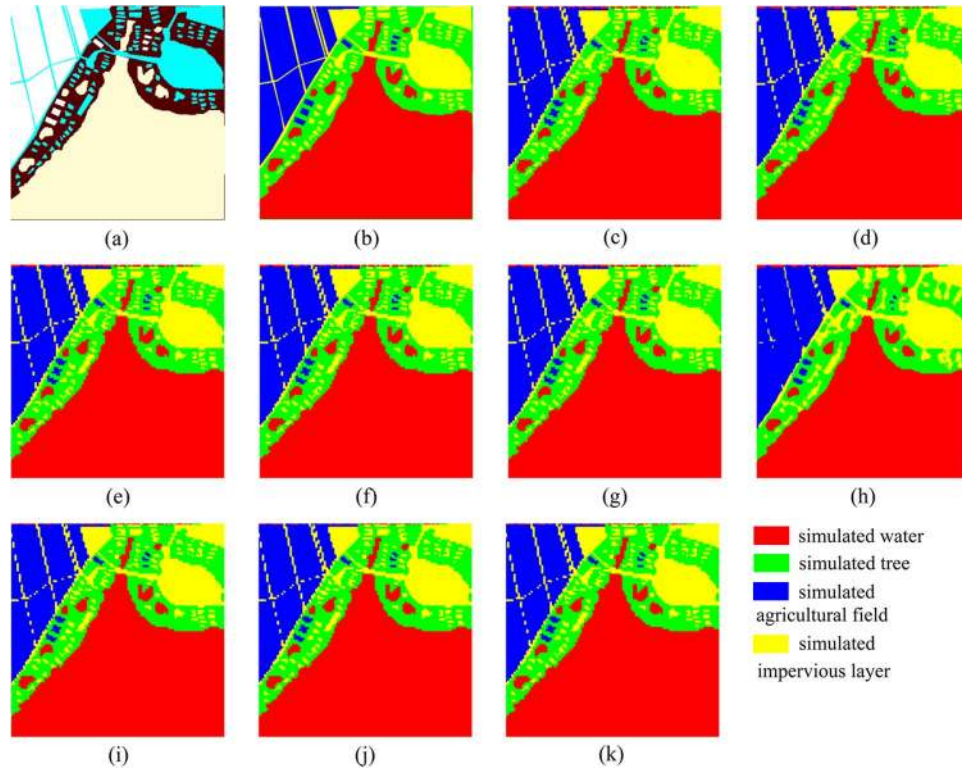
Fig. 6. Subpixel mapping results for the simulated hyperspectral data. (a) Original simulated hyperspectral image. (b) Reference classification map. (c) NNISM. (d) SASM. (e) PSSM. (f) BPSM. (g) GASM. (h) GSM. (i) AMCDSM-L. (j) AMCDSM-TV. (k) AMCDSM-BTV.

TABLE I
ACCURACY OF THE CLASSIFICATION RESULTS OF THE DIFFERENT METHODS FOR THE SIMULATED DATA

Method	NNISM	SASM	PSSM	BPSM	GASM	GSM	AMCDSM-L	AMCDSM-TV	AMCDSM-BTV
OA (%)	92.18	92.18	92.18	92.18	92.18	89.04	94.73	94.86	94.88
Kappa	0.8840	0.8840	0.8840	0.8840	0.8840	0.8379	0.9217	0.9237	0.9238

B. Experiment I—Simulated Image

In this experiment, a simulated image with 50 bands (400 × 400 pixels), created by using the USGS spectral library, was utilized to test the proposed algorithm. This image contains four land-cover classes—water, tree, agricultural field, and impervious layer (e.g., building and road)—as shown in Fig. 6(a).

A minimum-distance hard classification algorithm was applied to this simulated image to obtain the reference classification image, which is shown in Fig. 6(b). Fig. 6(c)–(k) shows the subpixel mapping results obtained by the NNISM, SASM, PSSM, BPSM, GSM, and proposed AMCDSM-L, AMCDSM-TV, and AMCDSM-BTV methods, respectively.

In this experiment, AMCDSM adaptively determined the regularization parameter, as described in Section III-C. As can be seen in Fig. 6, it can be observed that AMCDSM, as presented in Fig. 6(i)–(k), shows better subpixel mapping results than the other algorithms and adaptively obtains smoother visual results for all of the classes, using the spectral unmixing information while disregarding the abundance constraint. Serrated edges exist in the results generated by the traditional methods, and more subpixels are allocated to incorrect positions, as can be seen in Fig. 6(c)–(h). It is also worth noting that AMCDSM obtains better subpixel mapping results for the

two ridges of the field in the middle of the results than the other subpixel mapping algorithms.

For a more detailed verification of the results, the subpixel mapping results were compared with the hard classification result, and the accuracy of the results was assessed quantitatively, using OA and kappa, as shown in Table I. From Table I, we can see that the proposed method performs better and exhibits the highest accuracy values. GSM has the lowest accuracy because of the oversmoothing in the image. GASM is an optimization algorithm, and it can obtain a better subpixel mapping result by the use of evolution operators such as crossover and mutation. AMCDSM, as a novel subpixel mapping algorithm, has some major differences with GASM, e.g., in AMCDSM, prior models are used as the original input information, thus obtaining a better result. The OA values of AMCDSM-L, AMCDSM-TV, and AMCDSM-BTV are equal to 94.73%, 94.68%, and 94.88%, respectively, which is an improvement in the subpixel mapping accuracies of 2.55%, 2.68%, and 2.70% when compared with the most accurate traditional method. For the kappa index, the accuracies are 0.9217, 0.9237, and 0.9238, which is an improvement in the subpixel mapping accuracies of 0.0377, 0.0397, and 0.0398, respectively, when compared with the most accurate traditional method. Overall, the AMCDSM-BTV method obtains the best accuracy for this simulated data. The
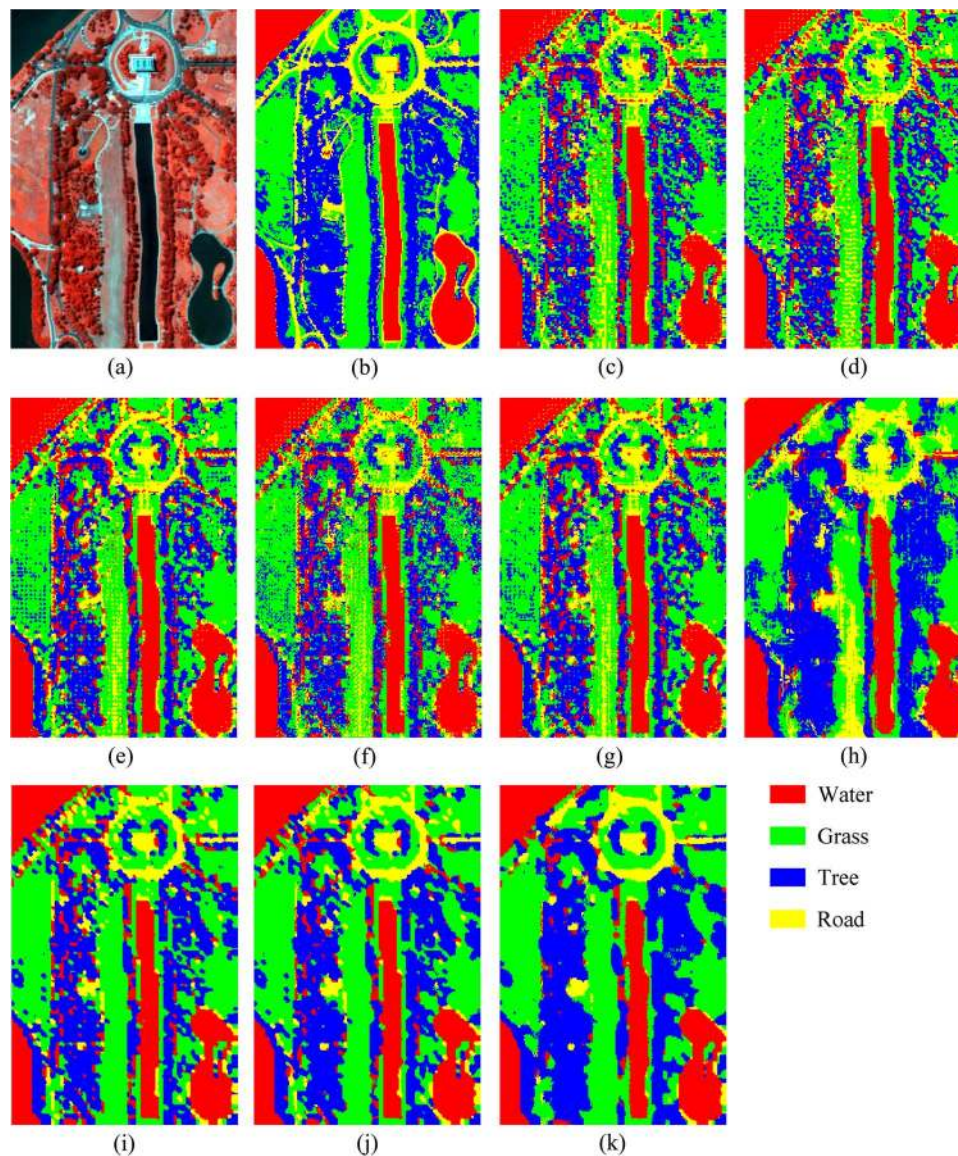
Fig. 7. Subpixel mapping results for the Washington DC image when using P-SVM for spectral unmixing. (a) Original hyperspectral image. (b) Reference classification map. (c) NNISM. (d) SASM. (e) PSSM. (f) BPSM. (g) GASM. (h) GSM. (i) AMCDSM-L. (j) AMCDSM-TV. (k) AMCDSM-BTV.

reason for this is that the BTV prior is derived from the TV prior by adding a bilateral filter, and it has the advantages of edge preservation and being computationally cheap to implement. The performance of AMCDSM-TV is similar to AMCDSM-BTV, owing to its ability to effectively preserve the edges and detailed information, while AMCDSM-L gives the worst result, compared with the other two priors, because of its high-pass operation and the smooth solution.

C. Experiment II—Synthetic Images

Three synthetic hyperspectral remote sensing images were used to test the performance of the proposed subpixel mapping algorithm in this experiment. Synthetic images can avoid the registration error between the low-resolution and HR images. Meanwhile, using synthetic images can also avoid the uncertainty inherent in real imagery that is caused by the sensor point spread function, atmospheric and geometric effects, and spectral unmixing or classification errors.

1) Synthetic Image—Washington DC HYDICE Image: In this experiment, an image that is a part of the Hyperspectral Digital Imagery Collection Experiment (HYDICE) airborne hyperspectral data set from the Washington DC Mall was utilized to test the proposed algorithm. This image has 191 bands, 300 lines, and 200 columns, and four categories of water, tree, road, and bare soil, as shown in Fig. 7(a), and it was used as the original image. Fig. 7(b) illustrates the reference image classified by the support vector machine (SVM) method, implemented by ENVI software [40]. The subpixel mapping scale was 4.

The subpixel mapping results of the different methods are displayed in Fig. 7(c)–(k), which illustrate the subpixel mapping results by the use of the NNISM, SASM, PSSM, BPSM, GSM, and proposed AMCDSM-L, AMCDSM-TV, and AMCDSM-BTV methods, respectively.

As can be seen in Fig. 7, a visual comparison suggests that the proposed method is successful in adaptively utilizing the fraction images obtained by the spectral unmixing to acquire the optimal results while disregarding the abundance constraint.

TABLE II
ACCURACY OF THE CLASSIFICATION RESULT OF THE DIFFERENT METHODS FOR THE WASHINGTON DC IMAGE

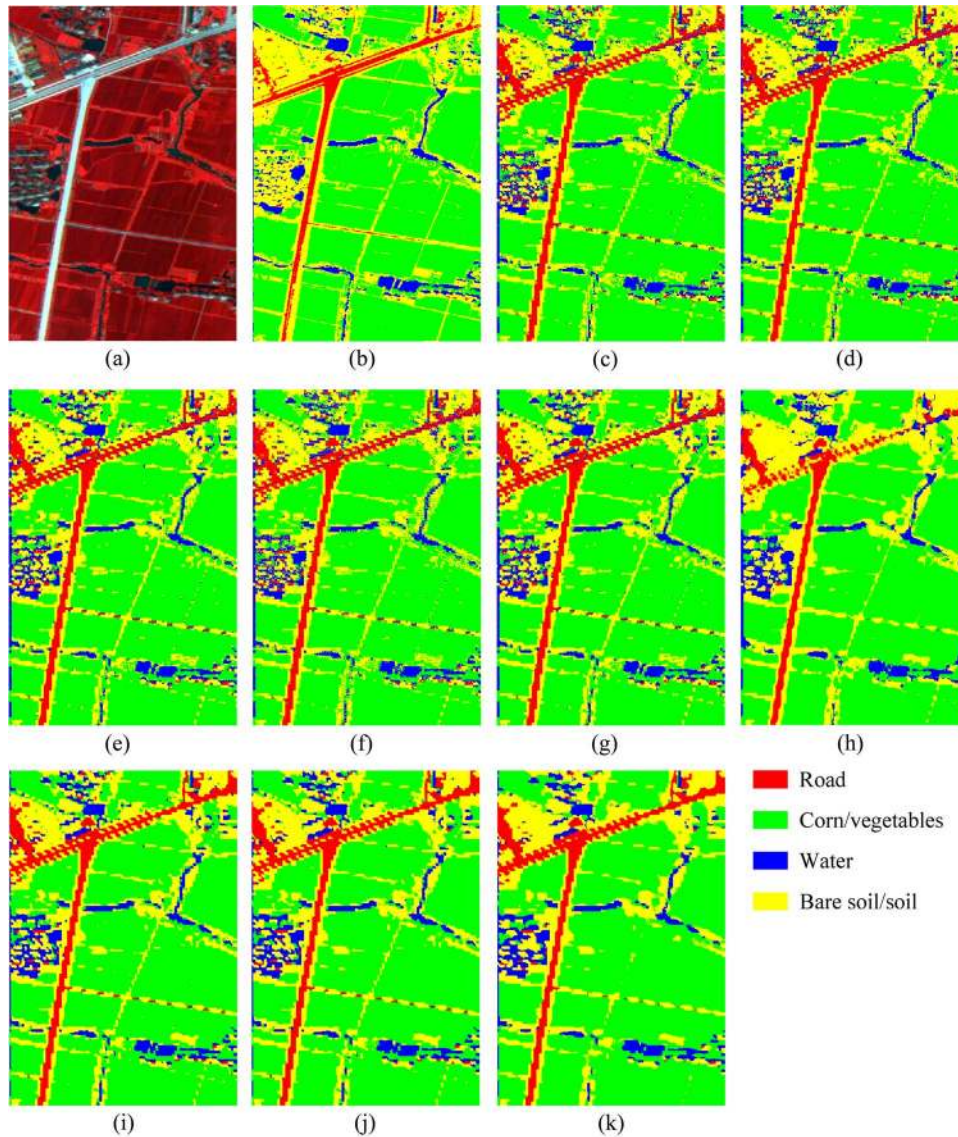| Method	NNISM	SASM	PSSM	BPSM	GASM	GSM	AMCDSM-L	AMCDSM-TV	AMCDSM-BTV
OA (%)	70.00	70.32	69.52	70.29	70.30	72.69	75.72	76.96	77.18
Kappa	0.5786	0.5831	0.5718	0.5826	0.5826	0.6109	0.6576	0.6733	0.6735

Fig. 8. Subpixel mapping results for the Xiaqiao image when using P-SVM for the spectral unmixing. (a) Original hyperspectral image. (b) Reference classification map. (c) NNISM. (d) SASM. (e) PSSM. (f) BPSM. (g) GASM. (h) GSM. (i) AMCDSM-L. (j) AMCDSM-TV. (k) AMCDSM-BTV.

From the comparison between Fig. 7(b) and (c)–(k), it can be seen that NNISM, SASM, PSSM, and BPSM do not provide satisfactory visual results, as there are lots of noisy points, and many subpixels of the images are allocated to incorrect positions, while GASM, GSM, AMCDSM-L, AMCDSM-TV, and AMCDSM-BTV obtain better results, being smoother and having better visual results. In particular, some tiny features, such as the boundary of the water at the bottom right of the reference classification image for the Washington DC data set, are not easily reconstructed using the traditional methods. However, the proposed method performs better by utilizing the adaptive MAP method while disregarding the abundance constraint.

For a more detailed verification of the results, a quantitative comparison of the aforementioned algorithms is shown in Table II. From Table II, we can conclude that the proposed AMCDSM method leads to a better performance than the other methods, and it improves the accuracy when compared with the other methods. For instance, the accuracies of AMCDSM-L, AMCDSM-TV, and AMCDSM-BTV are equal to 75.72%, 76.96%, and 77.18%, respectively, which is an improvement in the subpixel mapping accuracies of about 3.03%, 4.27%, and 4.49% when compared with the most accurate traditional method of GSM. For the kappa index, the accuracies are 0.6576, 0.6733, and 0.6735, which is an improvement in the

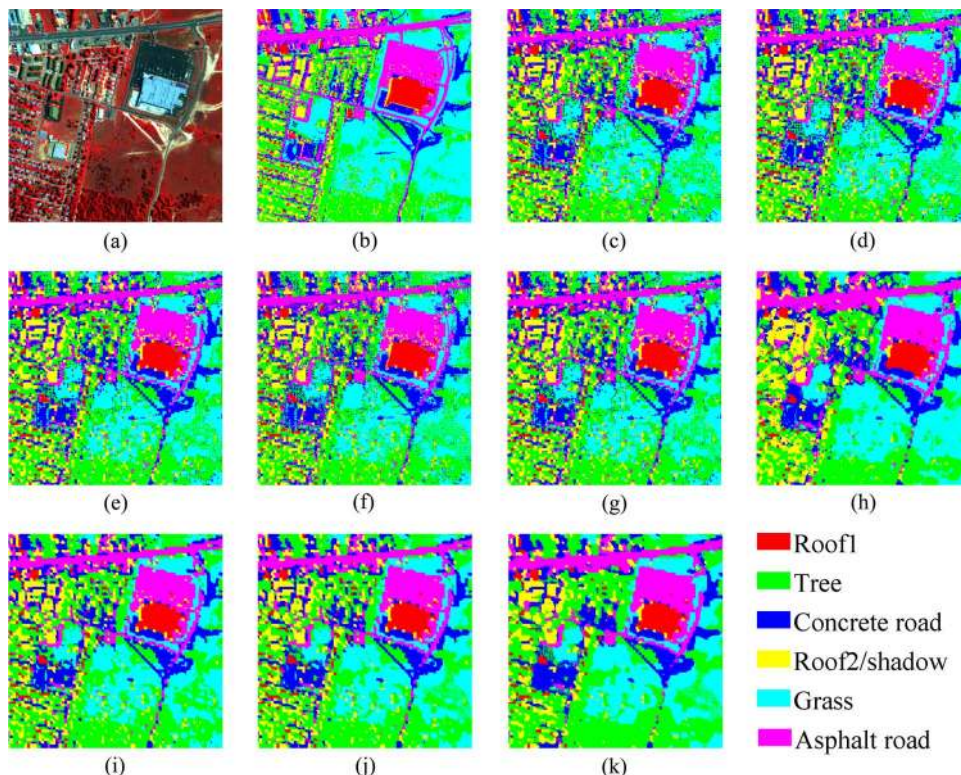| Method	NNISM	SASM	PSSM	BPSM	GASM	GSM	AMCD SM-L	AMCD SM-TV	AMCDS M-BTV
OA (%)	77.89	77.55	77.41	77.61	77.57	79.60	82.15	82.16	82.89
Kappa	0.5900	0.5837	0.5810	0.5848	0.5839	0.6193	0.6688	0.6684	0.6796

Fig. 9. Subpixel mapping results for the HYDICE urban image when using P-SVM for the spectral unmixing. (a) Original hyperspectral image. (b) Reference classification map. (c) NNISM. (d) SASM. (e) PSSM. (f) BPSM. (g) GASM. (h) GSM. (i) AMCDSM-L. (j) AMCDSM-TV. (k) AMCDSM-BTV.

subpixel mapping accuracies of 0.0467, 0.0624, and 0.0626, respectively, when compared with the most accurate traditional method of GSM. As with the simulated image, the AMCDSM-BTV method obtains the best accuracy. These experimental results demonstrate that the proposed approach outperforms the other algorithms for this data set.

2) Synthetic Image—Xiaqiao PHI Image: In this experiment, the proposed algorithm was tested with another hyperspectral image, which is a part of a remote sensing image collected with an airborne push-broom hyperspectral imager (PHI) from the Xiaqiao test site, China. A total of 78 bands of the PHI image (340×500 pixels) were used, and four classes of road, corn/vegetables, bare soil/soil, and water characterize this image, as shown in Fig. 8(a). Fig. 8(b) shows the reference image obtained by the SVM method. Fig. 8(c)–(k) illustrates the subpixel mapping results of the aforementioned methods. In this experiment, the scale factor was 4.

As can be seen in Fig. 8, as there are large areas of corn/vegetables, this image is not complex, and distinct differences between the classes can be observed. A very important feature in Fig. 8 is the road, and a visual comparison of this feature indicates that the proposed AMCDSM method obtains better visual subpixel mapping results. The proposed method is successful in adaptively utilizing the fraction images ob-tained by the spectral unmixing to acquire the optimal results while disregarding the abundance constraint. In order to better test the algorithms, a quantitative comparison is provided in Table III. Table III shows that the OA values of AMCDSM-L, AMCDSM-TV, and AMCDSM-BTV are equal to 82.15%, 82.16%, and 82.89%, respectively, which is an improvement in the subpixel mapping accuracies of 2.55%, 2.56%, and 3.29% when compared with the most accurate traditional method of GSM. The kappa values are 0.6688, 0.6684, and 0.6796 for the proposed method with the three prior models, which is an improvement in the accuracies of 0.0495, 0.0491, and 0.0603, respectively, when compared with the GSM method. As with the two previous images, the AMCDSM-BTV method obtains the best accuracy. As a result, the same conclusion can be drawn for the Xiaqiao data set, in that the proposed approach performs better than the other algorithms.

3) Synthetic Image—HYDICE Urban Image: In this experiment, a part of a HYDICE urban image was used. A total of 187 bands of the HYDICE image (300×300 pixels) were used, which contained six classes of roof1, tree, concrete road, roof2/shadow, grass, and asphalt road, as shown in Fig. 9(a). The scale factor was 4. Fig. 9(b) shows the reference classification data obtained by the SVM classifier. Fig. 9(c)–(k) displays the subpixel mapping results of the aforementioned methods.

TABLE IV
ACCURACY OF THE CLASSIFICATION RESULTS OF THE DIFFERENT METHODS FOR THE HYDICE URBAN IMAGE

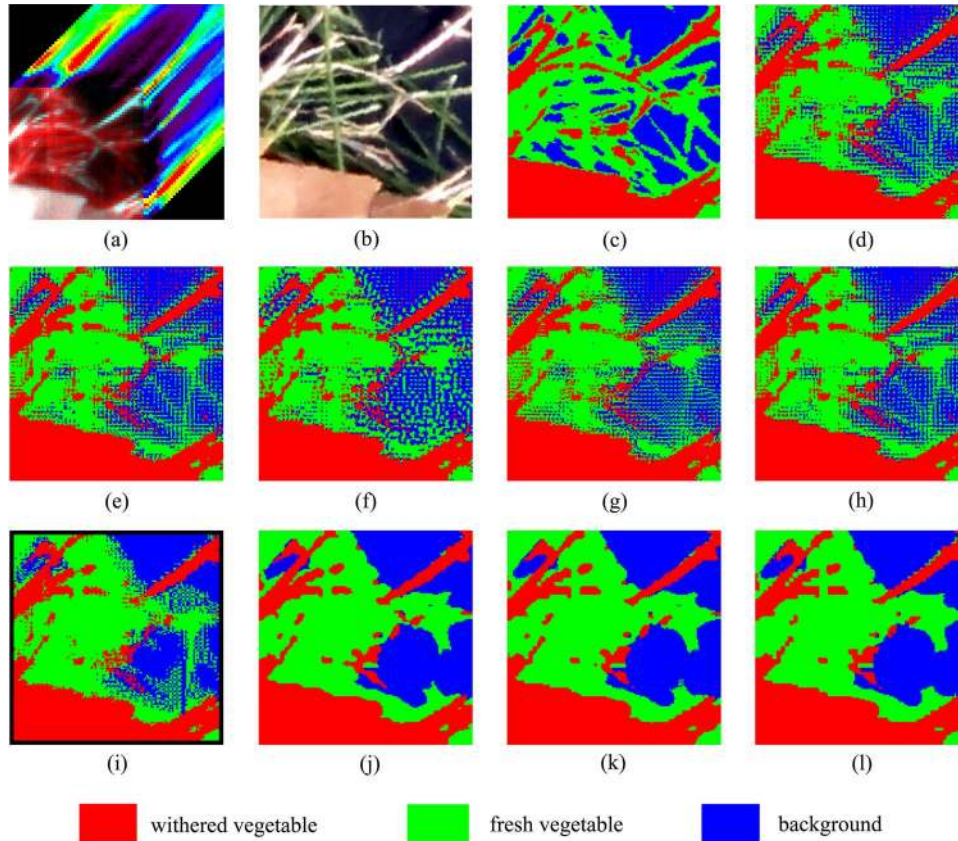| Method	NNISM	SASM	PSSM	BPSM	GASM	GSM	AMCDSM-L	AMCDSM-TV	AMCDSM-BTV
OA (%)	59.76	59.43	58.51	59.51	59.49	63.40	67.92	68.03	68.64
Kappa	0.4930	0.4888	0.4772	0.4898	0.4896	0.5369	0.5936	0.5947	0.6006

Fig. 10.   Subpixel mapping results for the Nuance hyperspectral image. (a) Base LR hyperspectral image. (b) HR color image. (c) Reference classification map obtained by SVM. (d) NNISM. (e) SASM. (f) PSSM. (g) BPSM. (h) GASM. (i) GSM. (j) AMCDSM-L. (k) AMCDSM-TV. (l) AMCDSM-BTV.

As can be seen in Fig. 9 and Table IV, AMCDSM obtains better results and the highest values of OA and kappa, which are equal to 67.92%, 68.03%, 68.64%, 0.5936, 0.5947, and 0.6006, respectively, which is due to the adaptability, the prior models, and the disregarding of the abundance constraint. The visual comparison shows that the roof1 feature has been better constructed than with the traditional methods. From the accuracy data presented in Table IV, we can clearly see that the proposed AMCDSM method improves the subpixel mapping performance when compared with the traditional methods. Among all of the methods, the AMCDSM-BTV method obtains the best accuracy. As this image has more categories than the aforementioned three images, the accuracies of the subpixel mapping results are a little lower than those for the previous experiments, but a similar conclusion can be drawn, which is that the proposed approach performs better than the other algorithms for this data set.

D. Experiment III—Real Nuance Image

To further evaluate the effectiveness of the proposed algorithm, an experiment with a real image was undertaken. This LR hyperspectral image (50×50) was collected using a Nuance NIR imaging spectrometer, while an HR color image (150×150) was simultaneously obtained by a digital camera for the same area. The scale factor here was 3. The image contained three classes: withered vegetable, fresh vegetable, and background. The reference classification map was obtained from an HR color image by the SVM classifier. Fig. 10(a)–(c) illustrates the base LR hyperspectral image, the HR color image, and the HR classification map, respectively. Fig. 10(d)–(l) shows the subpixel mapping results. Among the subpixel mapping results, the boundary of the image for GSM could not be handled as the scale was three; therefore, the accuracy evaluation was undertaken without the result from the edge.

Unlike the simulated image and the synthetic images, the real image contained more error sources, such as the registration error of the base LR image and the HR color image, the unmixing error of the LR image, and the classification error of the HR color image. Compared with the reference classification map, as displayed in Fig. 10, the results of the proposed method are again superior to the traditional methods. Unlike the other methods, which are seriously affected by the spectral unmixing error, AMCDSM overlooks the abundance constraint, thus

TABLE V
ACCURACY OF THE CLASSIFICATION RESULTS OF THE DIFFERENT METHODS FOR THE NUANCE IMAGE

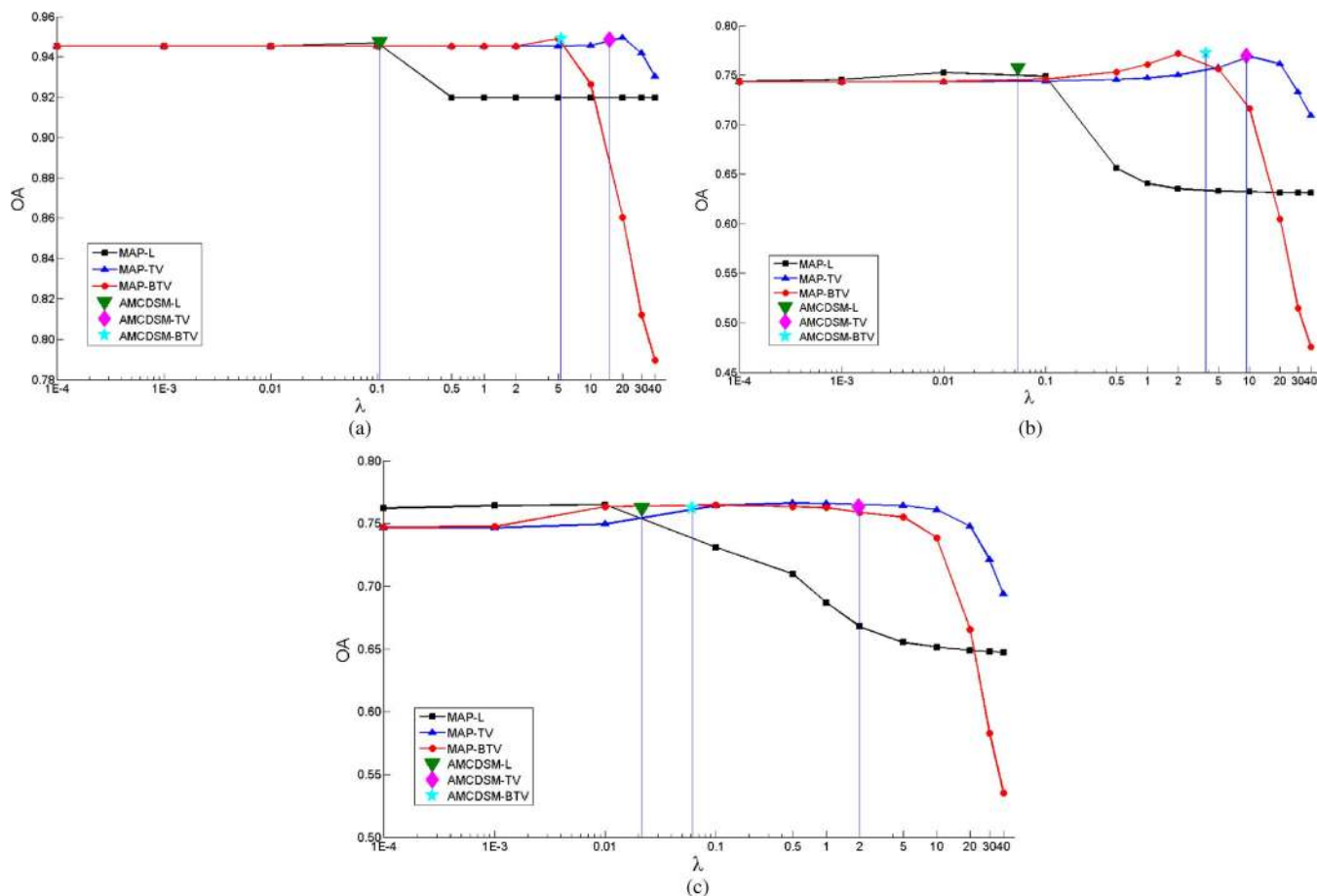| Method	NNISM	SASM	PSSM	BPSM	GASM	GSM	AMCD SM-L	AMCD SM-TV	AMCDS M-BTV
OA (%)	70.46	71.60	70.48	70.64	71.73	73.34	76.22	76.32	76.21
Kappa	0.5485	0.5660	0.5488	0.5512	0.5676	0.5892	0.6371	0.6382	0.6366

Fig. 11. Comparison of the proposed method with different prior models and regularization parameter values. (a) Simulated experiment. (b) Synthetic experiment with the DC image. (c) Real data experiment with the Nuance image.

obtaining a better result. It is, however, difficult to reach a balance between smoothing and detail preservation since smoothing can restrain the error of the spectral unmixing while eliminating the potential tiny features. Due to the scale being three and the fact that GSM does not deal with the boundary part, the accuracy is a little higher than the accuracies for the other methods, except for the proposed method. Due to the advantage of the MAP method, the proposed algorithm can obtain a better accuracy than the other methods, as is shown in Table V. The OA and kappa values of the AMCDSM-TV method are, respectively, about 4.59% and 0.0706 higher than the accuracy of the most accurate traditional method, GASM.

E. Sensitivity Analysis

As is known from (11) in Section III-A, the regularization parameter λ plays an important role in the iterative process, and it controls the balance between the data fidelity term and the prior term. If the parameter is too small, the noise cannot

be smoothed; however, if the parameter is too large, the image will become very blurred [42]. In order to test the performance of the proposed algorithm, the results obtained by the adaptive parameter are compared with the nonadaptive results of different values of the regularization parameter. The OA curves of the different parameter values with three priors and the adaptive results with three priors are plotted for the simulated image, DC image, and Nuance image and are shown in Fig. 11.

To compare the AMCDSM method with the nonadaptive MAP method, the best parameter λ value obtained in the nonadaptive MAP method must first be found. This parameter is not changed during the iterative process when using the nonadaptive MAP method. It can be seen from Fig. 11 that a series of regularization parameter values for the nonadaptive MAP method was set to find the most suitable one. For the same parameter values, the different prior models obtain different accuracies; however, for the same prior model, if the parameter values are different, the effect is not the same. As is shown, for the nonadaptive MAP method, when the value of λ is

small, the Laplacian prior gets the best accuracy. TV and BTV obtain the best results as the value of λ increases, while the Laplacian results decline to a steady state. Meanwhile, the accuracies of the three prior models all decrease greatly if λ exceeds a certain range. As was mentioned before and as is shown in Fig. 11(a)–(c), the optimum λ is obtained by the nonadaptive method, which is represented by the peak of the line. As the estimated lambda values obtained by the proposed adaptive method were updated in the iteration and the values were unfixed, we only show the final estimated lambda values in the iteration. As shown in Fig. 11(a)–(c), the estimated values are represented by different points using different shapes and colors and are denoted by the vertical lines. As shown in Fig. 11(a)–(c), for the AMCDSM method, the estimated optimum result, which was acquired adaptively, is almost the same as the optimum nonadaptive result, and the estimated lambda values are close to the manually selected ones; therefore, there is no need to set lots of parameter values to choose the best result. As can be seen in Fig. 11, the simulated image, the DC image, and the Nuance image all show similar patterns.

Consequently, we can conclude that the AMCDSM method is a feasible solution for subpixel mapping. It is easy to realize, and the optimum regularization parameter value can be adjusted in the iterative process.

V. Conclusion

In this paper, a novel adaptive subpixel mapping method based on a MAP model and a winner-take-all class determination strategy, namely, AMCDSM, has been proposed to adaptively deal with hyperspectral images by using original image downsampling and spectral unmixing to meet with the real situation. AMCDSM utilizes a MAP model, which has the ability to regularize the ill-posed problem by adding prior information to obtain a better subpixel mapping result. The traditional subpixel mapping algorithms always utilize the fraction image obtained by the classification image downsampling method as the input information. In AMCDSM, the original image downsampling and spectral unmixing results are applied to acquire the subpixel mapping result. Since the determination of the regularization parameter is very difficult, the traditional methods usually set a series of values to find the best result. In AMCDSM, an adaptive method is proposed to adaptively choose the optimal result, which is time-saving, simple, and efficient. As the spatial information between subpixels will be lost if the abundance constraint is strictly obeyed, the winner-take-all strategy chooses the largest value in the same position to be a certain category, thus avoiding the aforementioned problem. One simulated image, three synthetic images, and one real image were used to test the AMCDSM method and were compared with the traditional subpixel mapping methods. To better simulate a real situation, the abundance maps were acquired by the original image downsampling and spectral unmixing. The experimental results show that the AMCDSM algorithm consistently outperforms the previous subpixel mapping algorithms. In addition, the sensitivity analysis of the regularization parameter λ demonstrates that AMCDSM obtains similar results to the optimal parameters of manual selection

and hence provides an effective subpixel mapping method for hyperspectral remote sensing imagery.

References

[1] J. M. Bioucas-Dias et al., "Hyperspectral remote sensing data analysis and future challenges," IEEE Geosci. Remote Sens. Mag., vol. 1, no. 2, pp. 6–36, Jun. 2013.

[2] J. M. Bioucas-Dias et al., "Hyperspectral unmixing overview: Geometrical, statistical, and sparse regression-based approaches," IEEE J. Sel. Topics Appl. Earth Observ. Remote Sens., vol. 5, no. 2, pp. 354–379, Apr. 2012.

[3] X. Ceamanos et al., "Intercomparison and validation of techniques for spectral unmixing of hyperspectral images: A planetary case study," IEEE Trans. Geosci. Remote Sens., vol. 49, no. 11, pp. 4341–4358, Nov. 2011.

[4] R. Heylen, D. Burazerovic, and P. Scheunders, "Fully constrained least squares spectral unmixing by simplex projection," IEEE Trans. Geosci. Remote Sens., vol. 49, no. 11, pp. 4112–4122, Nov. 2011.

[5] M. D. Iordache, J. Bioucas-Dias, and A. Plaza, "Sparse unmixing of hyperspectral data," IEEE Trans. Geosci. Remote Sens., vol. 49, no. 6, pp. 2014–2039, Jun. 2011.

[6] P. M. Atkinson, "Mapping sub-pixel boundaries from remotely sensed images," in Innovations in GIS IV. London, U.K.: Taylor & Francis, 1997, ch. 12, pp. 166–180.

[7] P. M. Atkinson, M. Cutler, and H. G. Lewis, "Mapping sub-pixel proportional land cover with AVHRR imagery," Int. J. Remote Sens., vol. 18, no. 4, pp. 917–935, Mar. 1997.

[8] A. J. Tatem, H. G. Lewis, P. M. Atkinson, and M. S. Nixon, "Super-resolution target identification from remotely sensed images using a Hopfield neural network," IEEE Trans. Geosci. Remote Sens., vol. 39, no. 4, pp. 781–796, Apr. 2001.

[9] A. J. Tatem, H. G. Lewis, P. M. Atkinson, and M. S. Nixon, "Multiple-class land-cover mapping at the sub-pixel scale using a Hopfield neural network," Int. J. Appl. Earth Observ. Geoinf., vol. 3, no. 2, pp. 184–190, 2001.

[10] A. J. Tatem, H. G. Lewis, P. M. Atkinson, and M. S. Nixon, "Super-resolution land cover pattern prediction using a Hopfield neural network," Remote Sens. Environ., vol. 79, no. 1, pp. 1–14, Jan. 2002.

[11] Y. Su, G. Foody, A. Muad, and K. Cheng, "Combining Hopfield neural network and contouring methods to enhance super-resolution mapping," IEEE J. Sel. Topics Appl. Earth Observ. Remote Sens., vol. 5, no. 5, pp. 1403–1417, Oct. 2012.

[12] K. C. Mertens, L. P. C. Verbeke, T. Westra, and R. R. D. Wulf, "Sub-pixel mapping and sub-pixel sharpening using neural network predicted wavelet coefficients," Remote Sens. Environ., vol. 91, no. 2, pp. 225–236, May 2004.

[13] L. Zhang, K. Wu, Y. Zhong, and P. Li, "A new sub-pixel mapping algorithm based on a BP neural network with an observation model," Neurocomputing, vol. 71, no. 10–12, pp. 2046–2054, Jun. 2008.

[14] Y. Shao and R. S. Lunetta, "Sub-pixel mapping of tree canopy, impervious surfaces, and cropland in the Laurentian Great Lakes Basin using MODIS time-series data," IEEE J. Sel. Topics Appl. Earth Observ. Remote Sens., vol. 4, no. 2, pp. 336–347, Jun. 2011.

[15] J. Verhoeye and R. R. D. Wulf, "Land cover mapping at sub-pixel scales using linear optimization techniques," Remote Sens. Environ., vol. 79, no. 1, pp. 96–104, Jan. 2002.

[16] K. C. Mertens, B. D. Baets, L. P. C. Verbeke, and R. R. D. Wulf, "A sub-pixel mapping algorithm based on sub-pixel/pixel spatial attraction models," Int. J. Remote Sens., vol. 27, no. 15, pp. 3293–3310, Aug. 2006.

[17] P. M. Atkinson, "Sub-pixel target mapping from soft-classified, remotely sensed imagery," Photogramm. Eng. Remote Sens., vol. 71, no. 7, pp. 839–846, Jul. 2005.

[18] K. C. Mertens, L. P. C. Verbeke, E. I. Ducheyne, and R. R. D. Wulf, "Using genetic algorithms in sub-pixel mapping," *Int. J. Remote Sens.*, vol. 24, no. 21, pp. 4241–4247, Nov. 2003.

[19] Y. Zhong and L. Zhang, "Remote sensing image sub-pixel mapping based on adaptive differential evolution," *IEEE Trans. Syst., Man, Cybern. B, Cybern.*, vol. 42, no. 5, pp. 1306–1329, Oct. 2012.

[20] Y. Zhong and L. Zhang, "Sub-pixel mapping based on artificial immune systems for remote sensing imagery," *Pattern Recognit.*, vol. 46, no. 11, pp. 2902–2926, Nov. 2013.

[21] X. Xu, Y. Zhong, and L. Zhang, "Adaptive subpixel mapping based on a multiagent system for remote-sensing imagery," *IEEE Trans. Geosci. Remote Sens.*, vol. 52, no. 2, pp. 787–804, Feb. 2014.

[22] Q. M. Wang, L. G. Wang, and D. F. Liu, "Particle swarm optimization-based sub-pixel mapping for remote-sensing imagery," *Int. J. Remote Sens.*, vol. 33, no. 20, pp. 6480–6496, Oct. 2012.

[23] T. Kasetkasem, M. K. Arora, and P. K. Varshney, "Super-resolution land cover mapping using a Markov random field based approach," *Remote Sens. Environ.*, vol. 96, no. 3, pp. 302–314, Jun. 2005.

[24] V. A. Tolpekin and A. Stein, "Quantification of the effects of land-cover-class spectral separability on the accuracy of Markov-random-field-based superresolution mapping," *IEEE Trans. Geosci. Remote Sens.*, vol. 47, no. 9, pp. 3283–3297, Sep. 2009.

[25] L. Wang and Q. Wang, "Subpixel mapping using Markov random field with multiple spectral constraints from subpixel shifted remote sensing images," *IEEE Geosci. Remote Sens. Lett.*, vol. 10, no. 3, pp. 598–602, May 2013.

[26] A. Boucher and P. C. Kyriakidis, "Super-resolution land cover mapping with indicator geostatistics," *Remote Sens. Environ.*, vol. 104, no. 3, pp. 264–282, Oct. 2006.

[27] A. Boucher, P. C. Kyriakidis, and C. Cronkite-Ratcliff, "Geostatistical solutions for super-resolution land cover mapping," *IEEE Trans. Geosci. Remote Sens.*, vol. 46, no. 1, pp. 272–283, Jan. 2008.

[28] A. Boucher and P. C. Kyriakidis, "Integrating fine scale information in super-resolution land-cover mapping," *Photogramm. Eng. Remote Sens.*, vol. 73, no. 8, pp. 913–921, Aug. 2007.

[29] Y. Ge, S. Li, and V. C. Lakhan, "Development and testing of a subpixel mapping algorithm," *IEEE Trans. Geosci. Remote Sens.*, vol. 47, no. 7, pp. 2155–2164, Jul. 2009.

[30] F. Ling *et al.*, "Interpolation-based super-resolution land cover mapping," *Remote Sens. Lett.*, vol. 4, no. 7, pp. 629–638, Jul. 2013.

[31] Q. M. Nguyen, P. M. Atkinson, and H. G. Lewis, "Super resolution mapping using a Hopfield neural network with fused images," *IEEE Trans. Geosci. Remote Sens.*, vol. 44, no. 3, pp. 736–749, Mar. 2006.

[32] F. Ling, Y. Du, F. Xiao, H. Xue, and S. Wu, "Super-resolution land-cover mapping using multiple sub-pixel shifted remotely sensed images," *Int. J. Remote Sens.*, vol. 31, no. 19, pp. 5023–5040, Oct. 2010.

[33] X. Xu, Y. Zhong, L. Zhang, and H. Zhang, "Sub-pixel mapping based on a MAP model with multiple shifted hyperspectral imagery," *IEEE J. Sel. Topics Appl. Earth Observ. Remote Sens.*, vol. 6, no. 2, pp. 580–593, Apr. 2013.

[34] E. S. Lee and M. G. Kang, "Regularized adaptive high-resolution image reconstruction considering inaccurate subpixel registration," *IEEE Trans. Image Process.*, vol. 12, no. 7, pp. 826–837, Jul. 2003.

[35] M. Ng, H. Shen, E. Lam, and L. Zhang, "A total variation regularization based super resolution reconstruction algorithm for digital video," *EURASIP J. Adv. Signal Process.*, vol. 2007, no. 1, pp. 074585-1–074585-16, Jun. 2007.

[36] S. Farsiu, M. Robinson, M. Elad, and P. Milanfar, "Fast and robust multiframe super-resolution," *IEEE Trans. Image Process.*, vol. 13, no. 10, pp. 1327–1344, Oct. 2004.

[37] H. Shen, P. Li, L. Zhang, and Y. Zhao, "A MAP algorithm to super-resolution image reconstruction," in *Proc. IEEE 3rd Int. Conf. Image Graph.*, 2004, pp. 544–547.

[38] J. B. Adams, M. O. Smith, and P. E. Johnson, "Spectral mixture modeling: A new analysis of rock and soil types at the Viking Lander I site," *J. Geophys. Res.*, vol. 91, no. B8, pp. 8098–8112, Jul. 1986.

[39] P. Fisher, "The pixel: A snare and a delusion," *Int. J. Remote Sens.*, vol. 18, no. 3, pp. 679–685, Feb. 1997.

[40] American ITT Visual Information Solutions Company. *ENVI Online Tutorials* [EB/OL], 2014. [Online]. Available: http://www.exelisvis.com/ProductsServices/ENVIProducts/ENVI.aspx

[41] K. Wu, P. Li, and L. Zhang, "Sub-pixel mapping of remote sensing image based on MAP model," in *Proc. IEEE 4th Int. Conf. Image Graph.*, 2007, pp. 742–746.

[42] Q. Yuan, L. Zhang, H. Shen, and P. Li, "Adaptive multiple-frame image super-resolution based on U-curve," *IEEE Trans. Image Process.*, vol. 19, no. 12, pp. 3157–3170, Dec. 2010.

[43] A. Kanemura, S. Maeda, and S. Ishii, "Superresolution with compound Markov random fields via the variational EM algorithm," *Neural Netw.*, vol. 22, no. 7, pp. 1025–1034, Sep. 2009.

[44] R. R. Schultz and R. L. Stevenson, "Extraction of high-resolution frames from video sequences," *IEEE Trans. Image Process.*, vol. 5, no. 6, pp. 996–1011, Jun. 1996.

[45] L. Zhang, H. Zhang, H. Shen, and P. Li, "A super-resolution reconstruction algorithm for surveillance images," *Signal Process.*, vol. 90, no. 3, pp. 848–859, Mar. 2010.

[46] Y. Li, D. Dai, and L. Shen, "Multiframe super-resolution reconstruction using sparse directional regularization," *IEEE Trans. Circuits Syst. Video Technol.*, vol. 20, no. 7, pp. 945–956, Jul. 2010.

[47] X. Xu, Y. Zhong, and L. Zhang, "A sub-pixel mapping method based on an attraction model for multiple shifted remotely sensed images," *Neurocomputing*, vol. 134, pp. 79–91, Jun. 2014.

[48] K. Wu, L. Zhang, R. Niu, B. Du, and Y. Wang, "Super-resolution land-cover mapping based on the selective endmember spectral mixture model in hyperspectral imagery," *Opt. Eng.*, vol. 50, no. 12, pp. 126 201-1–126 201-14, Dec. 2011.

[49] A. Villa, J. Chanussot, J. A. Benediktsson, and C. Jutten, "Spectral unmixing for the classification of hyperspectral images at a finer spatial resolution," *IEEE J. Sel. Topics Signal Process.*, vol. 5, no. 3, pp. 521–533, Jun. 2011.

Yanfei Zhong (M'11) received the B.S. degree in information engineering and the Ph.D. degree in photogrammetry and remote sensing from Wuhan University, Wuhan, China, in 2002 and 2007, respectively.

He has been with the State Key Laboratory of Information Engineering in Surveying, Mapping and Remote Sensing, Wuhan University, since 2007, where he is currently a Professor. He has published more than 60 research papers, including more than 25 peer-reviewed articles in international journals such as the IEEE TRANSACTIONS ON GEOSCIENCE AND REMOTE SENSING, IEEE TRANSACTIONS ON SYSTEMS, MAN, AND CYBERNETICS—PART B, and *Pattern Recognition*. His research interests include multi- and hyperspectral remote sensing data processing, high-resolution image processing and scene analysis, and computational intelligence.

Dr. Zhong was the recipient of the National Excellent Doctoral Dissertation Award of China in 2009 and New Century Excellent Talents in University of China in 2009. He was a Referee of the IEEE TRANSACTIONS ON CYBERNETICS, IEEE TRANSACTIONS ON GEOSCIENCE AND REMOTE SENSING, IEEE JOURNAL OF SELECTED TOPICS IN APPLIED EARTH OBSERVATIONS AND REMOTE SENSING, IEEE GEOSCIENCE AND REMOTE SENSING LETTERS, and *Pattern Recognition*.

Yunyun Wu received the B.S. degree in remote sensing science and technology from the School of Geodesy and Geomatics, Jiangsu Normal University, Xuzhou, China, in 2012. She is currently working toward the M.S. degree in photogrammetry and remote sensing in the State Key Laboratory of Information Engineering in Surveying, Mapping and Remote Sensing, Wuhan University, Wuhan, China.

Her major research interests include multi- and hyperspectral remote sensing image processing.

Xiong Xu received the B.Sc. degree in photogrammetry and the Ph.D. degree in photogrammetry and remote sensing from Wuhan University, Wuhan, China, in 2008 and 2013, respectively.

He is currently a Research Assistant with the College of Surveying and Geo-informatics, Tongji University, Shanghai, China. His current research interests include multi- and hyperspectral image processing, artificial neural network, and pattern recognition.

Liangpei Zhang (M'06–SM'08) received the B.S. degree in physics from Hunan Normal University, Changsha, China, in 1982, the M.S. degree in optics from Xi'an Institute of Optics and Precision Mechanics, Chinese Academy of Sciences, Xi'an, China, in 1988, and the Ph.D. degree in photogrammetry and remote sensing from Wuhan University, Wuhan, China, in 1998.

He is currently the Head of the Remote Sensing Division, State Key Laboratory of Information Engineering in Surveying, Mapping and Remote Sensing, Wuhan University. He is also a "Chang-Jiang Scholar" Chair Professor appointed by the Ministry of Education of China. He is currently the Principal Scientist for the China State Key Basic Research Project (2011–2016) appointed by the Ministry of National Science and Technology of China to lead the remote sensing program in China. He is an Executive Member (Board of Governor) of the China National Committee of International Geosphere-Biosphere Programme. He also serves as an Associate Editor of the *International Journal of Ambient Computing and Intelligence*, *International Journal of Image and Graphics*, *International Journal of Digital Multimedia Broadcasting*, *Journal of Geo-spatial Information Science*, and *Journal of Remote Sensing*. He has more than 310 research papers and is the holder of 5 patents. His research interests include hyperspectral remote sensing, high-resolution remote sensing, image processing, and artificial intelligence.

Dr. Zhang is a Fellow of the Institution of Electrical Engineers, an Executive Member of the China Society of Image and Graphics, and others. He regularly serves as a Cochair of the series SPIE Conferences on Multispectral Image Processing and Pattern Recognition, Conference on Asia Remote Sensing, and many other conferences. He edits several conference proceedings, issues, and the Geoinformatics Symposiums. He is currently serving as an Associate Editor of the IEEE TRANSACTIONS ON GEOSCIENCE AND REMOTE SENSING.